

Supersonic nanoblowing: a new ultra-stiff phase of nylon 6 in 20–50 nm confinement

Cite this: *J. Mater. Chem. C*, 2013, **1**, 3491

Suman Sinha-Ray,^{†a} Min Wook Lee,^{†b} Sumit Sinha-Ray,^a Seongpil An,^b Behnam Pourdeyhimi,^c Sam S. Yoon^{*b} and Alexander L. Yarin^{*a}

The 20–50 nm nanofibers hold great promise as functional fabrics, biomedical materials, filters, fuel cell membranes, ultra-speed fiber optics, electronics and sensorics. In our novel process of supersonic solution blowing of nylon-6, 20–50 nm nanofibers are obtained. Here we found a new phase of nylon-6, which differs from the known α -, β -, γ -, δ - and λ -phases, presenting itself as a novel χ -phase. It is characterized by the decrease of CH₂ stretching, a shift of –NH stretching, a different type of hydrogen bond and a ten-fold increase in Young's modulus compared to those of post-processed macroscopic nylon fibers.

Received 6th February 2013
Accepted 3rd April 2013

DOI: 10.1039/c3tc30248b

www.rsc.org/MaterialsC

Introduction

The crystalline structure of polyamides, in particular, of nylon 6 has attracted much attention because of the importance of polyamides in many critical load bearing applications such as marine ropes, cords, air bags, seat belts, carpets, musical instruments, parachutes, flak vests, high performance fabrics, and as rubber reinforcement. The results of the X-ray analysis and modeling^{1,2} revealed two different stable crystal structures of nylon 6: α - and γ -phases. The monoclinic α -phase with hydrogen-bonded antiparallel fully extended chains appears when the nylon 6 melt gradually cools. On the other hand, the γ -phase with hydrogen-bonded parallel pleated chains appears when the nylon 6 melt is rapidly quenched. The α -phase is thermodynamically preferable, albeit formation of the γ -phase can be facilitated easier than the α -phase by an appropriate process route. Two intermediate crystal forms, β - and δ -phases, emerge as the α -phase transforms into the γ -phase and *vice versa*. The β - and δ -phases are unstable and have either different H-bond patterns or different chain conformations from the stable α - or γ -phases.

The smallest nanofibers in the range 20–50 nm cannot be obtained consistently by electrospinning³ and subsonic solution blowing,⁴ although they are of significant interest in areas of bio-separation, battery separators, and energy storage devices. Also, ordinary nanofibers in the range above 100–150

nm are intrinsically weak compared to the macroscopic post-treated fibers.³ Besides, there is an increasingly growing impetus in using nanofibers in portable electronics media (*e.g.* smartphones, MP3 players, headphones, laptops, hard drives, *etc.*) as a protective membrane against dirt, liquid, and airborne contaminants.^{5–8} The 20–50 nm nanofibers developed in the present work can become a breakthrough filter membrane in such applications due to their size. Such nanofibers would result in ultra-low penetration facemasks capable of removing nanoparticles smaller than 100 nm and airborne viruses without a significant increase in pressure drop, and effectively diminish incidence of seasonable epidemics of influenza, obstructive pulmonary diseases, fibrosis and lung cancer.^{6–8}

Here, we show that the novel method of the electrically assisted supersonic solution blowing results in an enormous stretching rate of nylon 6 on the order of 10^{10} s^{-1} . Such strong stretching of jets of nylon 6 solution in formic acid causes the macromolecular sheets, comprised of parallel molecular chains, to slide past each other in the stretching direction, diminishes the *d*-spacing to 0.156 nm, creates strong O...H bonding, and results in 20–50 nm diameter nanofibers with Young's modulus an order of magnitude higher than that of ordinary nylon 6 fibers.

Experimental

Electrically assisted supersonic solution blowing method

Compressed air extracted from a compressor with a stagnation pressure of $P_0 = 600 \text{ kPa}$ was supplied to the de Laval converging–diverging nozzle (*cf.* Fig. 1 and 2). This method is denoted as method A. The nozzle geometry was optimized to produce an exit pressure of $P_e = 101.3 \text{ kPa}$ to minimize the energy losses caused by shock waves. The nozzle throat and exit dimension were $d_t = 3 \text{ mm}$ and $d_e = 4.5 \text{ mm}$, respectively. Using

^aDepartment of Mech. & Ind. Eng., Univ. of Illinois at Chicago, Chicago, Illinois 60607-7022, USA. E-mail: ayarin@uic.edu; Fax: +1 312 413-0447; Tel: +1 312 996-3472

^bDepartment of Mechanical Engineering, Korea Univ., Seoul, 136-713 Korea. E-mail: skyoon@korea.ac.kr; Fax: +82 2 926-9290; Tel: +82 2 3290-3376

^c3427 The Nomwovens Institute, North Carolina State Univ., Box 8301, Raleigh, NC 27695-8301, USA

† Equal contribution.

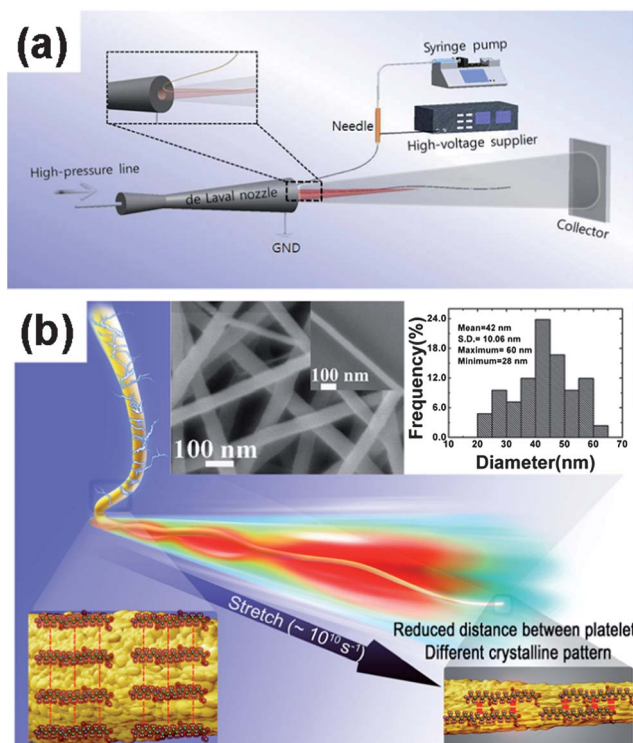


Fig. 1 Supersonic electrically assisted blowing and resulting nanofibers. (a) Schematic of the electrically assisted solution blowing setup. (b) Two-stage stretching of the polymer jet and crystal sheet alignment and packing. In the inset SEM images of nylon 6 nanofibers with a scale bar denoting 100 nm and size distribution are shown.

computational fluid dynamics, the flow speed at the nozzle exit was predicted to be around 558 m s^{-1} and the Mach number $M = 2.3$ (*cf.* Fig. 4a). Our experimental Schlieren images near the nozzle exit (Fig. 4d) also confirmed the supersonic speed of the gas as well as the presence of shock waves. Nylon 6 (Sigma Aldrich, molecular weight of repeat unit 104.83 Da), dissolved in formic acid (Sigma Aldrich) at 15 wt% was mixed for 24 h using a magnetic stirrer. A syringe pump (KDS LEGATO 100) supplied the mixed polymer solution to a stainless-steel needle (EFD, 25 gauge, with inner and outer diameters of 0.25 and 0.50 mm, respectively) at the flow rate of $Q = 100\text{--}200 \mu\text{l h}^{-1}$ with high DC voltage at the needle (Glassman High Voltage Inc., EL40P1). The electrically driven polymer jet was issued into the supersonic gas stream from the de Laval nozzle (Fig. 3a). Thinning jets inside the supersonic gas stream were monitored by a high-speed camera (Vision research Inc., Phantom 9.1) at a frame rate of ~ 2000 fps with LED lighting (50 W). The horizontal distance (S_1) and vertical distance (S_2) between the supersonic nozzle and the needle issuing polymer jets were set to 1.5 cm and 1.0 cm, respectively. The polymer jets were initially attracted toward the de Laval nozzle exit (upstream) which was grounded (Fig. 3a). However, the jets were abruptly bent downstream once the drag imposed by the supersonic gas stream became dominant (*cf.* Fig. 3). The distance between the nozzle exit and the collector substrate was 23.5 cm.

Another miniaturized setup was developed to exclude the compressor, which also required a smaller de Laval nozzle. This

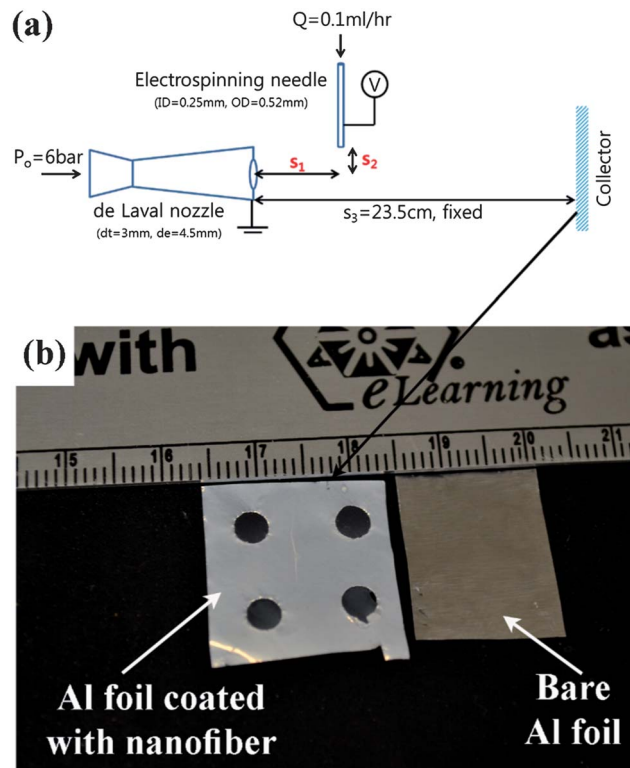


Fig. 2 (a) Detailed information on the electrically assisted solution blowing setup. (b) A macroscopically thick nanofiber sample collected on heavy-duty Al foil which became milky contrasted with a bare Al foil. The ruler above the samples is in cm.

method is denoted as method B. In this case, compressed air was supplied from the house pressure line at a supply (stagnation) pressure of 80 Psi (552 kPa), and the compressed air line was connected to the Silvent 209L de Laval nozzle. The air jet was supersonic up to a distance of 15 mm from the nozzle exit. All other process variables were kept as in method A; the polymer flow rate was $Q = 0.1 \text{ ml h}^{-1}$.

In both cases as the fiber collector, conductive materials such as aluminum foil, stainless steel and copper, as well as non-conducting materials such as glass and plastics were used. A plain impermeable sheet of the collector material was located on a rigid substrate and no backward flow resulting from the impinging gas jet was observed. The process could be continued as long as required and thick nanofiber mats were collected (*cf.* Fig. 2b).

Optical observations, Raman spectroscopy and differential scanning calorimetry

All SEM (Scanning Electron Microscopy) images were obtained using a JEOL-6320F after sputter coating the sample with Pt/Pd to a thickness of 7–8 nm. All TEM (Transmission Electron Microscopy) images were obtained using a JEOL JEM 3010. The TEM images were obtained using a holey carbon grid, whereas X-ray diffraction was done on nanofibers lying over a hole to avoid any possible interference from the background carbon grid. For TEM and small area electron diffraction (SAED) imaging a single nanofiber from a randomly oriented nanofiber mat was used. Raman Spectroscopy was done using a Renishaw

Raman scope 2000. Nanofibers were collected on an aluminum foil with punched holes of 5 mm diameter, and micro-Raman spectroscopy was conducted for the fiber samples suspended over the holes. Differential Scanning Calorimetry employed DSC 2010, TA Instruments.

Measurements of Young's modulus

Individual nanofibers were deposited across a trench (*cf.* Fig. 8). The tip of an atomic force microscope, AFM (XE-100, Park Systems, $R_{\text{tip}} = 10$ nm), pressed onto an individual fiber with force F , and the corresponding deflection δ was measured.

Results and discussion

Formation of 20–50 nm nanofibers

We developed a new process of fiber formation, in which an electrospun polymer jet is entrained in a supersonic gas flow from a de Laval nozzle (*cf.* Fig. 1a and 2a). Fig. 2a provides some details of the experimental setup. Fig. 2b shows a thick macroscopic sample collected on a perforated Al foil. For comparison a bare Al foil is also shown. It is seen that a thick nanofiber mat has a milky appearance, while the heavy-duty Al foil used as a convenient nanofiber collector displays a gray color. It is

emphasized that 20–50 nm nanofibers are practically transparent and only a thick mat comprised of them looks milky as in Fig. 2b.

Fig. 3a–d show the evolution of an electrified nylon 6 jet as it is attracted by electric forces to the exit of the de Laval nozzle and is abruptly swept from it by a supersonic gas stream. The numerically predicted structure of the electric field is shown in Fig. 3e. The results of the numerical simulations of the structure of the gas flow field are shown in Fig. 4a–c, and the corresponding measurement data (a Schlieren image) in Fig. 4d.

The mechanism of fiber formation under the combined action of an electric field and the supersonic jet, and the macromolecular sheet alignment are sketched in Fig. 1b, and it will be discussed in detail in the following section. To form these nanofibers, two different setups described above were used. The SEM images of an individual nylon 6 nanofiber and a nanofiber mat are shown in the inset in Fig. 1b with the fiber size distribution. A detailed information is presented in Fig. 5a–c. The results were highly reproducible irrespective of which setup (A or B) was used and 25G or 32G needle was used to issue the polymer jet. In the latter case the mean nanofiber diameter is 42 nm, with most of the fibers with diameters in the range 20 to 50 nm.

It is emphasized that all the size measurements were done using frames with more than 30 different nanofibers visible, which makes the results statistically sound and highly reproducible. When observing a 20–50 nm nanofiber, the depth of field of view is inevitably very small. This precludes “overall” measurements based on a zoomed-out view of an ensemble of fibers, since magnifications less than 35 000 \times inevitably cause significant errors related to the defocusing and astigmatism. That is why special care was taken to zoom-in and observe each fiber individually in such a way that only fibers lying almost in the same plane are measured. Fig. 5a–c show individual fibers in the middle and the “overall” views on the left. It is emphasized that the probability density functions of the fiber size distributions shown on the right in Fig. 5a–c were measured observing only individual fibers one by one and not the “overall” views, which are inevitably affected by the defocusing and astigmatism.

The ability to form seemingly defectless fibers (Fig. 5) in supersonic solution blowing stems from the high spinnability of viscoelastic polymer solutions in strong uniaxial elongation flows revealed in the recent theoretical/numerical and experimental works devoted to melt and solution blowing.^{4,9–13}

Jet stretching and alignment of crystal plates

When a jet of 15 wt% nylon 6 solution in formic acid is stretched from a needle of the exit diameter $d_n = 0.25$ mm (as for a 25G needle) and becomes a nanofiber of diameter $d_f \approx 50$ nm, a material element in the jet stretches $0.15(d_n/d_f)^2 \approx 10^7$ times, irrespective of whether it started stretching and shrinking from the needle exit or inside the needle. Therefore, the corresponding stretching ratio is of the order of 10^7 . For $d_n = 0.1$ mm (as for a 32G needle) and $d_f \approx 20$ nm the stretching ratio is even higher, of the order of 10^{10} . The entire stretching process takes about 1 ms (a conservative estimate based on the results of ref. 9–12 and 14), and thus the rate of strain is enormous, $\dot{\gamma} \approx 10^{10}$ s $^{-1}$ (even for the lowest value of the stretching ratio of 10^7).

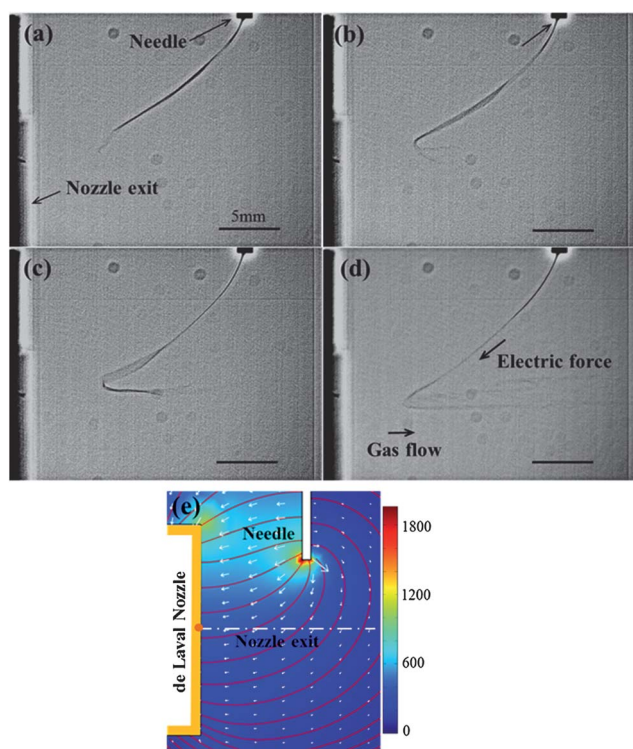


Fig. 3 Panels (a)–(d) show the evolution of a polymer jet issued from the high voltage needle and attracted to the grounded de Laval nozzle. The kink is caused by the supersonic gas jet. After the kink, the polymer jet already becomes so thin that it is invisible in the image. The needle's outer diameter in this case is 1.27 mm, and the time interval between the snapshots is $\Delta t = 0.5$ ms. A still insufficiently short exposition time results in a splaying-like optical artifact near the jet kink; in reality the jet is intact.^{4,9–12} Panel (e) shows the numerically simulated structure of the electric field between the high-voltage needle and the grounded de Laval nozzle. COMSOL software was used to predict the electric field. All scale bars are 5mm.

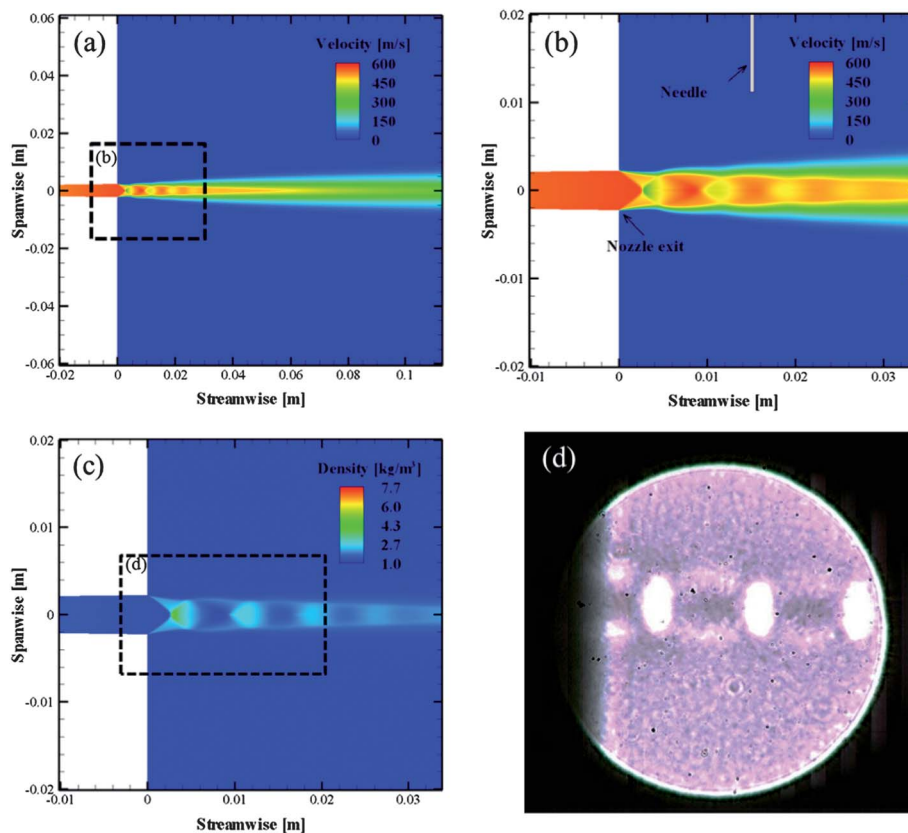


Fig. 4 (a)–(c) Supersonic gas flow. Panel (a) shows the velocity field in the gas. The rectangular area encompassed by the dashed line is shown in more detail in panel (b). Panel (c) shows the gas density field. Fluent 6.3 software was used in the numerical simulations of the gas flow field. Panel (d) shows the Schlieren image (the gas density difference) corresponding to the rectangular area encompassed by the dashed line in panel (c).

It was shown that macromolecular chains of nylon 6 always self-organize in a narrow confinement as pretty rigid sheets.² In solution these sheets can slide until the polymer jet is fully dried. Formic acid, being a good solvent for nylon 6, facilitates sheet sliding. When a material element of a polymer jet undergoes stretching at a stretching rate $\dot{\gamma}$, macromolecular sheets comprised of nylon 6 chains move according to the following equation:

$$\frac{dx}{dt} = \dot{\gamma}x \quad (1)$$

where x is the position of the center of mass of a macromolecular sheet, and t is the time.

The probability of finding a macromolecular sheet at a certain position x in the material element at time t , $W(x,t)$ satisfies the following Fokker–Planck equation

$$\frac{\partial W}{\partial t} + \dot{\gamma}x \frac{\partial W}{\partial x} = -\dot{\gamma}W \quad (2)$$

with the solution

$$W(x,t) = e^{-\dot{\gamma}t} W_0(xe^{-\dot{\gamma}t}) \quad (3)$$

where $W_0(\cdot)$ is the initial probability distribution of the macromolecular sheets, which can be taken as a Gaussian distribution. Then, eqn (3) becomes

$$W(x,t) = \exp(-\dot{\gamma}t) \frac{1}{\sqrt{2\pi}\sigma} \exp\left[-\frac{(x \exp(-\dot{\gamma}t))^2}{2\sigma^2}\right] \quad (4)$$

where σ is the standard deviation.

As time increases, any sharp initial distribution rapidly widens according to eqn (4), and the macromolecular sheets are scattered wider along the fiber axis, with the longitudinal order fading. The enormous stretching rate in the present process accelerates such macromolecular sheet realignment and packing beyond the rate achieved in electrospinning where $\dot{\gamma} \approx 10^3 \text{ s}^{-1}$ (ref. 14 and 15). The enormous macromolecular sheet sliding disrupts all the inter-sheet H-bonds, since the energy provided by the surrounding gas flow is sufficient for that as the estimate in the following section shows. As a result, the re-assembled phase of nylon 6 becomes different from the α -phase and acquires stronger hydrogen bonds, which would be impossible in standard crystal phases of nylon 6 owing to conformational hindrances. Under such strong uniaxial stretching, the methylene segments move, the solvent rapidly evaporates, hydrogen bonds hold the macromolecular sheets and then, stop their movement to form a new crystalline structure, the χ -phase. That is how the lateral ordering in the polymer jet happens and the order parameter is the final inter-sheet distance, which is associated in this particular case with d -spacing. In the subsequent sections the existence of the novel χ -phase will be shown through various characterizations.

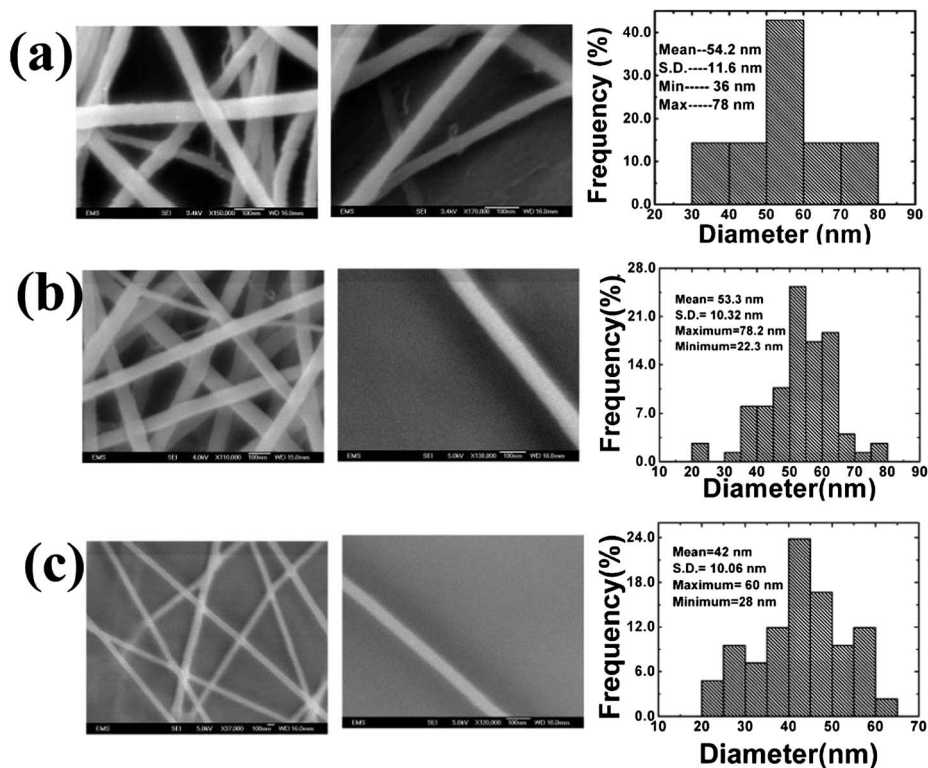


Fig. 5 (Left) “overall” SEM images of nanofiber mats. (Middle) individual nanofibers. (Right) probability density function of the fiber size distribution. (a) 25G needle was used; method A. (b) 25G needle was used; method B. (c) 32G needle was used; method B.

Novel χ -phase

TEM images of a single 50 nm nanofiber are shown in Fig. 6a and c, and the corresponding X-ray diffraction patterns in Fig. 6b and d, respectively. The diffraction patterns reveal several important features: a single sharp ring, which indicates no α -phase in the nanofiber, which corresponds to doublet rings indexed as (200) and (002)/(202) reflections.² The diffraction patterns in Fig. 6b and d do not correspond to the γ -phase, which would be indicated by doublet rings indexed as (020) and (001).^{2,16–19} For comparison, in electrospun nylon 6 fibers, equatorial reflections assigned to the γ -phase lattice planes associated with (200) and (011) reflection planes and meridional reflections associated with the (020) reflection plane were observed,¹⁹ in distinction from a single ring in Fig. 6b and d. The existence of a single ring shows that these nanofibers did not contain the λ -phase observed in nylon oligomers²⁰ or the δ -phase.²¹ From Fig. 6b and d, the d -spacing is 0.156 nm, which is much smaller than those for the α -phase, which are 0.432 nm and 0.385 nm, and for the γ -phase, which is 0.413 nm.^{22,23} Therefore, the present nanofibers do not consist of the α -, γ -, δ -, and λ -phases. The C–C bonds of length 0.154 nm are located in the sheet planes, whereas a d -spacing of 0.156 nm signifies the inter-sheet distance. This corresponds to the fact that there is no ordering in the longitudinal direction, because otherwise a sharp ring corresponding to a d -spacing larger than the C–C bond length would have appeared in Fig. 6b and d.

The specific energy required to break all the inter-sheet bonds between two parallel macromolecular sheets located at

the d -spacing of 0.156 nm is evaluated as $E_H = A/(12\pi d^2)$, where A is the Hamaker constant. Taking for the estimate $A = 0.5 \times 10^{-19}$ J, we find $E_H = 54.5$ mJ m⁻². On the other hand, the

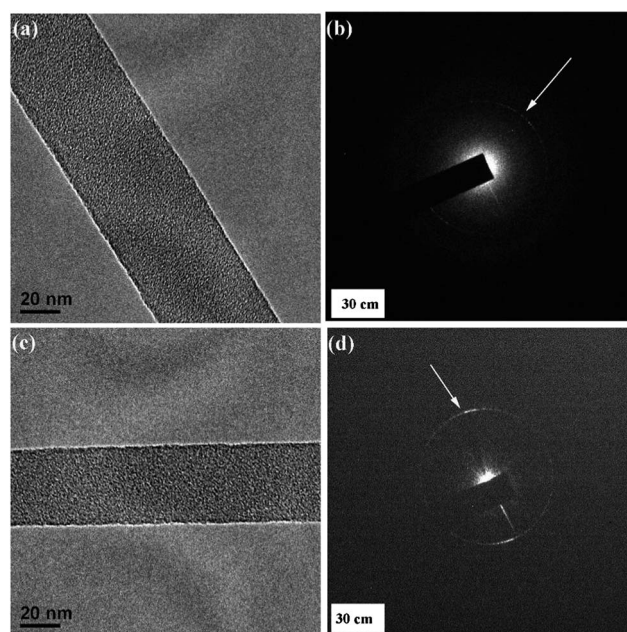


Fig. 6 TEM images of two different nanofibers are shown in panels (a) and (c), and the corresponding small area electron diffraction (SAED) pattern in panels (b) and (d). In panels (b) and (d), the arrows point at the brightest spot on the rings. In panels (b) and (d), the written value (30 cm) indicates the camera distance.

specific energy transferred to the polymer jet from the surrounding gas jet is of the order of $E_G = 100\rho_G U^2 a$ where ρ_G is the gas density, U is the relative velocity of the polymer and gas jets, and a is the cross-sectional radius of the polymer jet.¹² Taking for the estimate $\rho_G = 1 \text{ kg m}^{-3}$, $U = 600 \text{ m s}^{-1}$, and $a = 10^{-2} \text{ cm}$ (as in the initial part of the polymer jet), we obtain $E_G = 3600 \text{ J m}^{-2} \gg E_H$. When the polymer jet radius diminishes to 20 nm, $E_G = 720 \text{ mJ m}^{-2} > E_H$. In both cases the energy supplied by the gas jet is quite sufficient to break all the inter-sheet bonds and result in sliding of macromolecular sheets.

The existence of a sharp ring reveals that the fibers in Fig. 6 are not amorphous; if they were, a diffuse ring would appear. It is still possible that the fiber is comprised of the intermediary metastable β -phase.^{1,19} The typical diffraction pattern (Fig. 6b and d) shows that the ring is the sharpest in the direction approximately perpendicular to the direction of fiber orientation, which means that the macromolecular sheets are aligned along the fiber.

Differential scanning calorimetry (DSC) was applied to nanofibers to compare them with the parent polymer pellet (Fig. 7a–d). The thermograms of the original pellet and the resulting nanofibers were significantly different. It can be seen that during the first stage of heating (Fig. 7b), the nanofibers undergo glass transition in the temperature range 45–125 °C, whereas the pellet undergoes glass transition in the temperature range 165–205 °C. The fact that the nanofibers have a significantly lower glass transition temperature range than the corresponding bulk polymer is verified from ref. 24. For the β -phase, an exothermal recrystallisation peak at 55 °C was reported for nylon 6 in ref. 25, where cast films from the β crystal-dominated samples were studied. The absence of any exothermal peak in Fig. 7 shows that neither the parent pellet nor the nanofibers are comprised of the β -phase in the present case. The absence of any exothermal peak for the nanofibers at 55 °C and the appearance of an endothermic peak instead are very instructive and unusual. In Fig. 7b, a broad exothermic rise is seen at 125–185 °C for

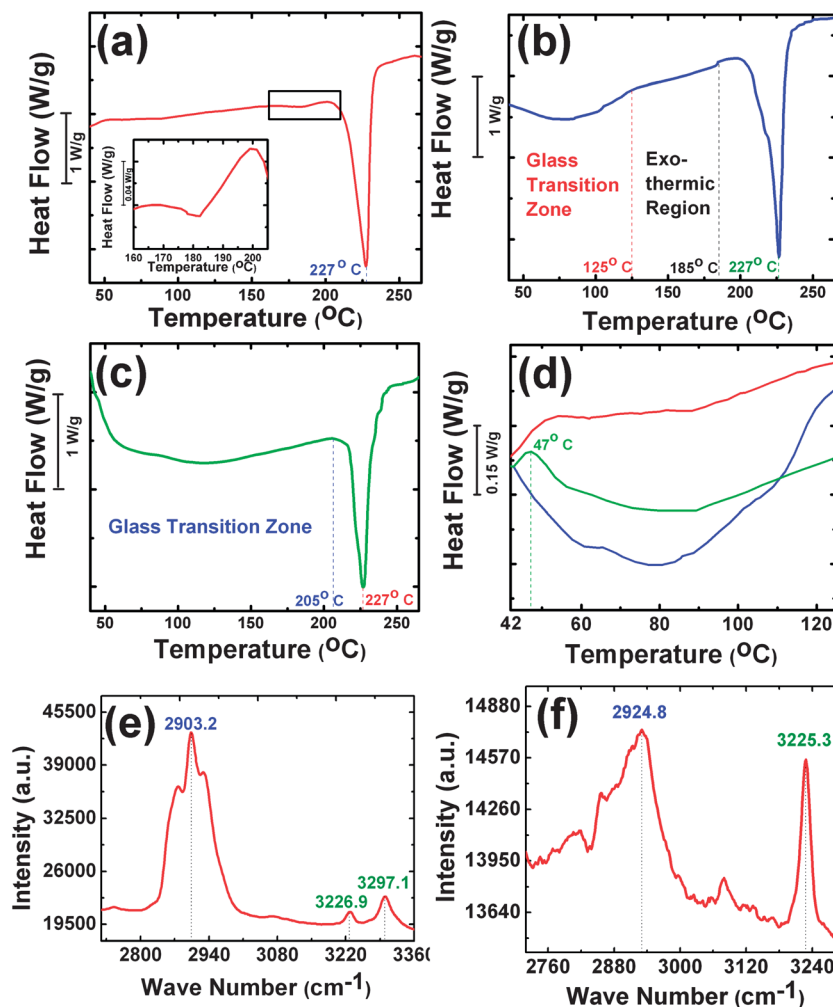


Fig. 7 DSC thermograms of (a) nylon 6 pellet, (b) nanofiber mat undergoing the 1st cycle of heating, (c) nanofiber mat undergoing the 2nd cycle of heating, and (d) zoomed-in view of panels (a)–(c) at a low temperature range with the line colors corresponding to the respective DSC plots in panels (a)–(c). In panel (a) in the inset, a zoomed-in view of the glass transition zone is shown. After the 1st heating cycle, the nanofiber sample was cooled down and then subjected to the 2nd heating cycle. Panels (e) and (f) show the micro-Raman spectroscopy results of the nylon 6 pellet and the 50 nm nanofiber mat, respectively. The blue values indicate the wavenumbers corresponding to $-\text{CH}_2$ stretching and the green values indicate the wavenumber corresponding to $-\text{NH}$ stretching.

nanofibers that underwent the 1st cycle of heating, originating from a complete or partial restructuring of the material into a more stable phase (most probably, the α -phase). Indeed, the DSC thermogram of nanofibers that underwent the 2nd heating cycle (Fig. 7c) shows features visible in both DSC thermograms in panels (a) and (b), *i.e.* already a mixture of two phases, the χ - and α -phases. The co-existence of these two crystalline phases can be also traced in the lower temperature range (42–125 °C; Fig. 7d), where the DSC thermogram of the nanofibers that underwent the 2nd heating cycle lies in-between the data for the pellet and for the nanofibers that underwent the 1st heating cycle. In summary, the results shown in Fig. 7 exclude the last previously known β -phase in nanofibers.

Fig. 7a–c also show that both nanofibers and pellet melt at almost the same temperature of 227 °C. It is known that bigger electrospun nanofibers have a significantly lower melt temperature than the parent bulk polymers.²⁴ Then, the data in Fig. 7 imply that the crystal phase in the present 20–50 nm nanofibers has a melt temperature significantly higher than the α -phase in the pellet ($T_m = 227$ °C).

The nature of H-bonds in the crystal phases was explored by micro-Raman spectroscopy of a pellet (Fig. 7e) and nanofibers (Fig. 7f). For nylon 6, the range 2853–2920 cm^{-1} corresponds to CH_2 stretching, and 3300 cm^{-1} corresponds to N–H stretching.²⁶ The peak corresponding to CH_2 stretching shifted from 2903.2 cm^{-1} for the pellet to 2924.8 cm^{-1} for the nanofibers. In Fig. 7e, in addition to the peak at 3297.1 cm^{-1} there is another small peak at 3226.3 cm^{-1} . This additional peak at 3226.3 cm^{-1} corresponds to the shift in the N–H stretch caused by pressing during the manufacturing stage (ref. 27). However, in the nanofibers, the N–H stretch peak shifts to 3225.3 cm^{-1} (Fig. 7f). The fiber diameter is reduced in the millisecond range from ~ 1 mm at the needle to a final value of about 50 nm at a stretching rate on the order of 10^{10} s^{-1} (*cf.* Fig. 3) and by squeezing macromolecular sheets in the radial direction. The distance between the electronegative atoms N and O in the bond structure of $\text{C}=\text{O}\cdots\text{H}-\text{N}$ decreases, and the $\text{O}\cdots\text{H}$ bond becomes stronger. This weakens the NH– bond, as well as shifts NH stretch towards a lower wavenumber. Then, a $-\text{CH}_2$ group of one chain is forced to move closer to a $-\text{CH}_2$ group of a neighboring chain, with the corresponding decrease in the mean C–H bond distance and the increase in the H–C–H angle. The increased angle leads to a shift of the CH_2 stretching mode and the decrease of the axisymmetric stretching mode. Fig. 6b

and d reveal that the d -spacing is significantly lower than those of the standard crystal phases of nylon 6. In addition to the hydrogen bonds within the same macromolecular sheet, inter-sheet hydrogen bonds can also form in the present case. The existence of stronger $\text{O}\cdots\text{H}$ bonds supports this conjecture.

The stronger $\text{O}\cdots\text{H}$ bond should result in unusually stiff nanofibers. The results of the nano-indentation experiment were processed using the formulae based on the Euler-Bernoulli bar bending theory (ref. 28, p. 94, ref. 29–31) in the limit of small deflections

$$E = \frac{FL^3}{192I\delta}, \quad E = \frac{FL^3}{48I\delta} \quad (5)$$

where I is the cross-sectional moment of inertia, and L is the length of the suspended fiber. The first equation of eqn (5) implies clamp conditions on both sides, while the second equation implies the zero-moment conditions, which are the two limiting cases.

It is emphasized that the high tension acquired when fibers are stretched in flight relaxes, since they are deposited at the wafer in a semi-wet state and thus possess enough time (more than about 0.01 s which is the characteristic relaxation time) for viscoelastic relaxation.³² As for the effect of the tension potentially developed in bending, the estimate based on the standard theory of bending²⁸ shows that it can be neglected if $(d/\delta)^2 > 1$, where d is the fiber cross-sectional diameter and δ is the bending deflection. In our work $d \sim 50$ nm, $\delta \leq 17$ nm, and thus $(d/\delta)^2$ is of the order of 10. Therefore, eqn (5) is fully valid.

The values of E which were obtained using eqn (5) were 11.51 GPa and 46.04 GPa, respectively (*cf.* Fig. 8), which is significantly higher than $E = 2$ –3.5 GPa of ordinary macroscopic post-treated nylon 6 fibers. Note that there were reports that stiffness of electrospun nanofibers increases when their cross-sectional diameter decreases below 150 nm.^{15,33} For polyacrylonitrile nanofibers that was attributed to low crystallinity which results from rapid solvent evaporation and solidification.³³ In the present case of even smaller nylon 6 nanofibers this factor is also present, albeit the fibers are not amorphous and contain a new phase, which can be responsible for the enhanced stiffness. In the past, formation of the extended-chain crystals in electrospun poly(ethylene oxide) nanofibers was reported,³⁴ which shows that strong uniaxial elongational flows of polymer solutions accompanying nanofiber formation are capable of producing new crystalline phases.

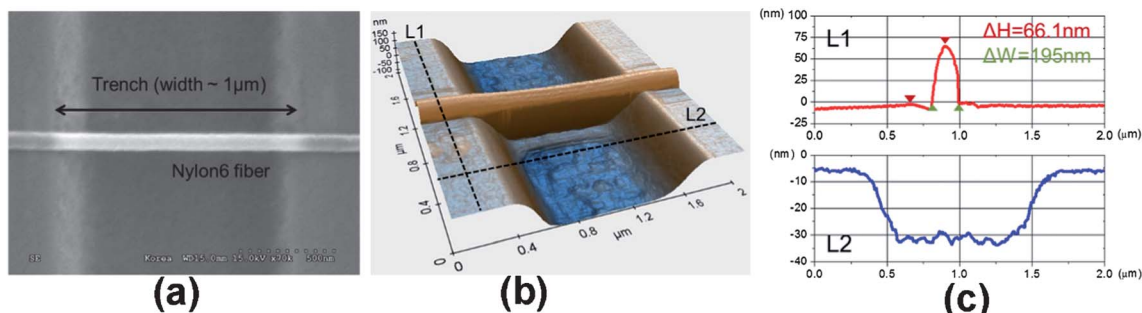


Fig. 8 (a) A nanofiber deposited across a trench for measurement of Young's modulus, (b) AFM landscape of the fiber and trench, and (c) fiber and trench profiles.

Conclusions

The electrostatically assisted solution blowing allows one to achieve enormous stretching rates of the order of 10^{10} s^{-1} . This results in the formation of nylon 6 nanofibers with the mean diameters close to 50 nm, with most of the fibers being in the range 20 to 50 nm. In such confinements under the conditions of rapid solidification on the scale of 1 ms, nylon 6 forms a new crystalline χ -phase with significantly enhanced hydrogen bonds. As a result, the as-spun nanofibers reveal Young's modulus in the range 11.51–46.04 GPa, an order of magnitude higher than that of macroscopic post-treated fibers. Formation of nanofibers in the range 20 to 50 nm, which are subjected to the van der Waals forces, holds great promise for the development of novel gecko-like nano-textured adhesives, which can find use, in particular, in facemasks and other biomedical materials. One layer of such nanofibers sandwiched in the filter medium is expected to significantly improve the filtration performance. In general, formation of novel crystalline phases of other polymers by means of supersonic electrically assisted solution blowing might be expected.

Acknowledgements

Drs Alan Nicholls' and Ke-bin Low's help with electron microscopy and Raman Spectroscopy is greatly appreciated. This work was also supported by the National Research Foundation of Korea (2012-0001169, 2011-0030433, and 2010-0010217), and the Converging Research Center Program (2010K000969). This work is chosen for support by the Nonwovens Cooperative Research Center (NCRC).

References

- 1 Y. Li and W. A. Goddard III, *Macromolecules*, 2002, **35**, 8440.
- 2 D. R. Holmes, C. W. Bunn and D. J. Smith, *J. Polym. Sci.*, 1955, **17**, 159.
- 3 E. Zussman, M. Burman, A. L. Yarin, R. Khalfin and Y. Cohen, *J. Polym. Sci., Part B: Polym. Phys.*, 2006, **44**, 1482.
- 4 S. Sinha-Ray, A. L. Yarin and B. Pourdeyhimi, *Carbon*, 2010, **48**, 3575.
- 5 <http://www.donaldson.com/en/micro/literature/055390.pdf>.
- 6 W. Yang, S. Elankumaran and L. C. Marr, *J. R. Soc., Interface*, 2011, **8**, 1176.
- 7 C. Wang and Y. Otani, *Ind. Eng. Chem. Res.*, 2013, **52**, 5.
- 8 Y. Filatov, A. Budyka and V. Kirichenko, *Electrospinning of Micro- and Nanofibers: Fundamentals and Applications in Separation and Filtration Processes*, Begell House, 2007.
- 9 S. Sinha-Ray, Y. Zhang, A. L. Yarin, S. Davis and B. Pourdeyhimi, *Biomacromolecules*, 2011, **12**, 2357.
- 10 S. Sinha-Ray, A. L. Yarin and B. Pourdeyhimi, *J. Appl. Phys.*, 2010, **108**, 034912.
- 11 A. L. Yarin, S. Sinha-Ray and B. Pourdeyhimi, *J. Appl. Phys.*, 2010, **108**, 034913.
- 12 A. L. Yarin, S. Sinha-Ray and B. Pourdeyhimi, *Polymer*, 2011, **52**, 2929.
- 13 S. Khansari, S. Sinha-Ray, A. L. Yarin and B. Pourdeyhimi, *J. Appl. Phys.*, 2012, **111**, 044906.
- 14 D. H. Reneker, A. L. Yarin, H. Fong and S. Koombhongse, *J. Appl. Phys.*, 2000, **87**, 4531.
- 15 A. Arinstein, M. Burman, O. Gendelman and E. Zussman, *Nat. Nanotechnol.*, 2007, **2**, 59.
- 16 J. C. Ho and K. W. Wei, *Macromolecules*, 2000, **33**, 5181.
- 17 J. Schultz, B. Hsiao and J. S. Amon, *Polymer*, 2000, **41**, 8887.
- 18 C. Ramesh and E. B. Gowd, *Macromolecules*, 2001, **34**, 3308.
- 19 Z. Zhao, W. Zheng, H. Tian, W. Yu, D. Han and B. Li, *Mater. Lett.*, 2007, **61**, 925.
- 20 R. Dersch, T. Liu, A. K. Schaper, A. Greiner and J. H. Wendorff, *J. Polym. Sci., Part A: Polym. Chem.*, 2003, **41**, 545.
- 21 P. Sikorski and E. D. T. Atkins, *Macromolecules*, 2001, **34**, 4788.
- 22 B. L. Murphy and R. G. Kuhn, *Can. Publ. Pol.*, 2002, **XXVII**, 249.
- 23 D. P. Russell and P. W. R. Beaumont, *J. Mater. Sci.*, 1980, **15**, 197.
- 24 R. Srikar, T. Gambaryan-Roisman, C. Steffes, P. Stephan, C. Tropea and A. L. Yarin, *Int. J. Heat Mass Transfer*, 2009, **52**, 5814.
- 25 L. Penel-Pieron, C. Depecker, R. Seguela and J.-M. Lefebvre, *J. Polym. Sci., Part B: Polym. Phys.*, 2001, **39**, 484.
- 26 W. F. Maddams and I. A. M. Royaud, *Spectrochim. Acta, Part A*, 1991, **47**, 1327.
- 27 J. Reynolds and S. S. Sternstein, *J. Chem. Phys.*, 1964, **41**, 47.
- 28 L. D. Landau and E. M. Lifshitz, *Theory of Elasticity*, Pergamon Press, 1970.
- 29 M. K. Shin, S. I. Kim, S. J. Kim, H. Lee and G. M. Spinks, *Appl. Phys. Lett.*, 2006, **89**, 231929.
- 30 M. B. Bazbouz and G. K. Stylos, *J. Polym. Sci., Part B: Polym. Phys.*, 2010, **48**, 1719.
- 31 U. Stachewicz, R. J. Bailey, W. Wang and A. H. Barber, *Polymer*, 2012, **53**, 5132.
- 32 D. H. Reneker, A. L. Yarin, E. Zussman and H. Xu, *Adv. Appl. Mech.*, 2007, **41**, 43.
- 33 D. Papkov, Y. Zou, M. N. Andalib, A. Goponenko, S. Z. D. Cheng and Y. A. Dzenis, *ACS Nano*, 2013, DOI: 10.1021/nn400028p.
- 34 E. Zussman, D. Rittel and A. L. Yarin, *Appl. Phys. Lett.*, 2003, **82**, 3958.